Losses in Grid and Inverter Supplied Induction Machine Drives

T.C. Green, C.A. Hernández-Arámburo and A.C. Smith*

Department of Electrical and Electronic Engineering
Imperial College London
South Kensington Campus
London SW7 2AZ

*Department of Electrical and Electronic Engineering
UMIST
PO Box 88
Manchester M60 1QD

Losses in Grid and Inverter Supplied Induction Machine Drives

1 Abstract

Inverter supply is known to create additional power losses in an induction machine over those occurring with grid supply. The extent and nature of that increase is examined here for a switching frequency representative of current practice. Data is obtained from a time-stepped finite element analysis (FEA) model of the machine coupled to circuit equations that include a model of the switching action of the inverter. A variable time-step algorithm is employed to ensure accurate representation of the switching waveforms at reasonable computational effort. Further improvement in speed is achieved by not performing a full FEA update of elemental reluctivities at every time-step but instead only when required by a change in magnetic flux.

The power loss found in simulation is verified through experimental tests for both the machine and inverter. The examination of losses categorises those losses by cause, location and frequency band. The causes modelled are motor ohmic and iron losses and inverter conduction and switching losses. Iron losses are further divided into hysteresis, classic eddy-current and anomalous losses. Pulse-width modulation (PWM) at 5 kHz gave an identifiable but relatively unimportant increase in ohmic loss in the machine. In contrast, iron losses increased significantly. Eddy current loss in the rotor increased significantly (by up to 150% near the head of the bar) while in the stator, a significant increase in iron loss was caused by the phase-band leakage flux generated at the switching frequency.

2 Introduction

Induction machine drives using PWM inverters are common place and range from simple drives where variable speed aids efficiency to high performance servo systems. De-rating of an induction machine for use with an inverter was common when inverter switching frequencies were low and the consequent harmonic distortion of the supply voltage large [1]. The question now arises as to whether there are significant additional losses in an induction machines when supplied by modern high switching frequency inverters that are free of low-order voltage distortion. The overall loss performance of the machine can be tested experimentally but for a

detailed answer to the question, a simulation of the various loss components is needed. There are three difficulties in performing this simulation. First, the available models for iron loss are not well advanced; second, the data for such models is derived in the main from low frequency tests, and third, the time-step simulations are computationally expensive when conducted with the small time-steps necessary for high switching frequency waveforms. A good understanding of how and where losses develop is important in designing efficient induction motors for use with inverters and so the study is worth pursuing despite these difficulties.

There have been many studies of iron loss in induction machines. The well known equivalent circuit [2] has been modified in various ways to improve the accuracy of the loss estimate for wide ranges of operating conditions such as in [3]. Iron loss models suitable for use in *dq*-models of the induction machine have also been studied [4,5]. These lumped models of iron loss are useful but do not allow the detail of the iron loss to be studied. Some studies have specifically addressed losses arising from inverter supply [6,7] but are limited in nature.

There are models for iron loss in thin laminations, equations 1-4, [8]. These models provide loss density results for a localised flux density expressed as a function of time. The power density can be integrated over the area of the lamination (and multiplied by the effective stack length) to provide the power loss or can be used to provide maps of the loss distribution. This loss model has been used in conjunction with time-step finite element analysis techniques [9]. The FEA yields the flux density in each element at each time-step. Equations 1-4 can then be applied in a post processing step.

$$P_{iron} = l_{Stack} \int_{Lam\ Area} \left\{ P_{hyst}^{density} + P_{eddy}^{density} + P_{anom}^{density} \right\} dS \qquad (1)$$

$$P_{hyst}^{density} = k_{Laver} \frac{k_{1hyst}}{T} B_{pk}^{\ k_{2hyst}}$$

$$k_{Laver} = 1 + \frac{k_{3hyst}}{B^{pk}} \sum_{i}^{N} \Delta B_i \qquad (2)$$

$$P_{eddy}^{density} = \frac{\sigma \delta^2}{12} \cdot \frac{1}{T} \int^{T} \left(\frac{\partial B}{\partial t} \right)^2 .dt \qquad (3)$$

$$P_{anom}^{density} = k_{anom} \frac{1}{T} \int_{0}^{T} \left| \frac{\partial B}{\partial t} \right|^{\frac{3}{2}} .dt \qquad (4)$$

Where:

P_{iron} is the iron power loss [W]

$P_{hyst}^{density}$ is the hysteresis power loss density [W/m^3]

$P_{eddy}^{density}$ is the classic eddy current power loss density [W/m^3]

$P_{anom}^{density}$ is the anomalous power loss density [W/m^3]

B is the flux density [T]

B_{pk} is the peak flux density [T]

ΔB_i is the amplitude of the i^{th} minor flux loop [T]

N is the number of minor flux loops

T is the period of the fundamental waveform [s]

k_{1hys} is the hysteresis loss linear constant

k_{2hys} is the hysteresis loss exponential constant

k_{Laver} is Laver's correction factor for minor loops

k_{3hys} is the hysteresis loss minor-loop weighing constant

k_{anom} is the anomalous loss constant

σ is the lamination conductivity [S/m]

δ is the lamination thickness [m]

The iron loss model was applied separately to the orthogonal (tangential and radial) components to flux that the power losses summed. In other words, no specific procedure was applied to account for rotational losses. It is believed that this approach will lead to an over estimate to the total iron loss because rotational losses are less than the sum of losses from separate orthogonal fields [10]. This is the case for many, but not all, of the conditions found in a machine lamination. A paper examining this issue (and using the example machine used here) is currently under review [11].

The FEA model linking the flux developed in the machine to the current excitation must be coupled to a circuit model linking the current that flows to the applied stator voltages and the voltages induced by the rate of change of flux linkage. Several approaches have been reported. It

is possible to form a joint solution matrix [12] or to incorporate the circuit equations into an eddy-current formulation of the magnetic problem [13]. The approach adopted here follows Williamson and his co-workers [14] and uses time-stepping of an equivalent circuit in which the mutual inductance matrix is obtained from FEA.

The aim of the work here is to adapt the time-stepped finite element method to make it suitable and accurate for use with realistically high inverter switching-frequencies. The results are then verified against experimental tests. Once verified, the method will be used to examine how and where an inverter increases losses in an induction machine.

3 Simulation System

Time-step FEA simulation has been applied to inverter waveforms but these studies were restricted to simple six-step (quasi-square wave) inverters [15, 16] or PWM inverters with low switching frequencies [16, 17, 18]. With a low switching frequency it is possible, but not particularly accurate, to use a fixed time-step. The time-step has to be sufficiently small such that the important detail of the PWM waveform is captured. It is worth remarking that the information contained in a PWM waveform is in the form of the timing of its edges and not its amplitude. The time-step should be around $1/100^{th}$ of the PWM period (the sample frequency should be 100 times the switching frequency) to represent accurately the waveform and avoid significant aliasing (in a situation where other anti-alias precautions are difficult). This is a large and unnecessary computational effort that can not be sustained for realistically high switching frequencies. The PWM information is best captured by using variable time-steps aligned to the durations of the states of the inverter. A three-phase inverter has 8 possible states (ignoring the under-lap condition) of which 4 are used in any one PWM cycle. Two states are repeated in each cycle and so 6 state durations are used. The average sample frequency will be 6 times the switching frequency. Even so, the computational effort required to simulate one complete cycle of rotor current is very large. For a rotor current of 0.5 Hz and a switching frequency of 20 kHz, 240,000 time-steps will be required. If fixed time-steps were used something in the region of 4 million steps would be required.

Time-stepping the equivalent circuit portion of the Williamson model is relatively fast. The time consuming stage is, naturally, the FEA used to obtain the mutual inductance matrix. The Williamson model allows these two tasks to be decoupled and separately considered. The

equivalent circuit must be updated at each change of inverter state. The mutual inductance matrix can be updated selectively. Two factors cause the matrix to change over time: rotation of the rotor and changes in magnetic saturation. Rotation of the rotor by a small angle (as over one time-step) can be dealt with by holding the elemental reluctivities constant and rotating the rotor mesh. The reluctivities of the elements need only be updated using FEA as the magnetic conditions dictate. A non-linear time-step involves an iterative solution of the both the equivalent circuit and the finite element model so that agreement is reached on the 3 stator and 2 rotor currents. A linear time-step involves only the time-stepping of the equivalent circuit. The numerical integration of the equivalent circuit equations is performed in terms of the flux-linkages, $\boldsymbol{\psi}$ not the currents, $\mathbf{I}$. The currents are obtained by multiplying by the inverse of the mutual inductance matrix, L^{-1}, equations 5 and 6.

$$\frac{d\boldsymbol{\psi}(t)}{dt} = V_{DC} \times \mathbf{S}_{Inv}^{k} - \mathbf{V}_{Si}(\mathbf{I}) - \mathbf{R}\,\mathbf{I} \qquad (5)$$

$$\mathbf{I} = \mathbf{L}^{-1}\,\boldsymbol{\psi} \qquad (6)$$

where V_{DC} is the DC-link voltage,

$\mathbf{S}_{Inv}^{k}$ is the switch-state vector for the inverter state, and

$\mathbf{V}_{Si}(\mathbf{I})$ is the voltage drop across the semiconductors of the inverter as a function of current.

The current vector is composed of three stator currents and two (*d* and *q*) rotor currents in this implementation. Only the fundamental space harmonic distribution of rotor current was considered. Rotor currents were modelled as uniform across the bar cross-section although the skin effect increase in resistance with frequency is applied later when calculating rotor ohmic power loss following a frequency decomposition of the current.

The switch-state vector for a star-connected machine would take values of ±1 according to the state of each leg of the inverter; for the delta connected machine used here it takes values of +1, 0 or -1 depending on the states of two inverter legs.

Generally, several linear time-steps were conducted between non-linear time-steps and thus a large saving in computation effort is made. Certain precautions were necessary to ensure accuracy of this technique with variable time-steps.

- Time-steps were arranged to start and end at precisely the instant where the inverter changes state (*i.e.,* one or more phase legs switch)
- If the duration of an inverter state exceeded a threshold it was divided into two or more linear time-steps otherwise it was left as one time-step.
- Non-linear solutions were forced after the appropriate accumulated time. Normally, non-linear solutions are aligned to existing time-steps but extra solution points are forced if no convenient time-step exists. These extra time-steps enable low switching frequencies to be simulated without compromising the accuracy of the machine model.
- If a very short duration inverter state caused a very short time-step just ahead of a non-linear solution, the non-linear solution was delayed until after a longer time-step. Without this precaution, all of the non-linear aspect of the change in flux occurs over the short time-step. This makes little difference to the flux density results but would cause erroneously large time derivatives of the flux density.

The last of these precautions is particularly important for accurate calculation of iron losses although it may not appear to make much difference to flux density results themselves. If the change in flux due to a reluctivity update is allocated to a small time step then there is a large rate-of-change of flux which can make a large difference to the iron loss calculation. Another way of looking at this is that spurious high frequency components can introduced by the reluctivity update. However, it is the rate-of-change of flux, rather than the flux this is most pertinent to the discussion of iron loss.

The iron losses were assessed from the flux density and time derivative of the flux density of each element after the simulation run had completed. Ohmic losses (here taken to mean losses in the conductors of stator and rotor, *i.e.*, not including eddy current loss) were assessed from the current data. The stator was assumed to be wound from sufficiently thin wire to be able to neglect skin effect. Skin effect in the rotor end-rings and bars was accounted for by a simple correction factor to the DC rotor resistance and rotor leakage inductance [3].

4 Experimental System

To verify the simulation models developed in the previous sections, a series of tests were conducted on a 4-pole, 2.1 kW induction machine. The machine had a delta connected stator winding rated for 240 V (line) operation and was housed in a D100 fully enclosed case. The machine operates with a slip of 0.05 at rated voltage and power. Some indicative dimensions of

the machine are included later in figure 11 but other details are subject to commercial confidentially. An unusual feature of this test machine was that the rotor is un-skewed. This was a deliberate decision so that a multi-slice skew model would not be needed for the simulation. It does, however, mean that slotting components are at higher magnitude than in a standard industrial design machine. The machine was supplied from a standard 415 V, 50 Hz, three-phase supply via a VARIAC or from an IGBT inverter. The inverter operated from a DC-link of 400 V, the switching frequency was 5 kHz and for this study the inverter was arranged to give the same open-circuit fundamental voltage and frequency as the grid supply. Power losses were not directly measured (by a calorimeter for instance) but instead assessed through the difference between output power and input power. A 3-phase power analyser suitable for PWM signals was used to measure DC-link power and inverter output power with an accuracy of 2 % of the rated input power. Machine output power was measured with an in-shaft torque sensor (accurate to ±0.25 Nm) and speed pick-up from a 1024-line encoder (which after sampling gave a resolution of 1 r.p.m.). Mechanical load was provided by DC machine. Frictional losses in the induction machine were separately assessed with the DC machine excited as a motor and with the induction machine unexcited. The measured mechanical power during testing was then adjusted for friction. A block diagram of the experimental system is shown in figure 1.

Thermocouples were embedded in the stator windings of the induction machine so that the machine could be elevated to a known temperature (through loaded running) prior to taking a set of data. All tests were conducted with the stator windings at 70ºC.

5 Verification of Total Losses

The experimental conditions described in Section 4 were replicated in the simulation. It was not possible to measure the rotor temperature so, following practice sometimes followed in design of small machines, the rotor end-rings were assumed to be 10ºC hotter than the stator winding and the rotor bars to be 20ºC hotter. The magnetic characteristics of the steel were taken from manufacturer's data. To overcome the difference between a particular machine and the data from a typical (and un-worked) sample of steel, data of the *B-H* curve were scaled (while preserving the smoothness of the curve) until the no-load (magnetising) current found by simulation at a range of voltages was in agreement with experimental data. This was a trail-and-error process. Voltage drop and switching energy data for the IGBTs and diodes of the inverter was taken from manufacturer's quoted typical data.

As a confidence check, the stator current found in simulation was compared with the values measured in the experimental system. Figure 2 shows these results plotted against slip for both grid and inverter operation. Note that un-normalised slip (*i.e.,* f_S - f_R) is used for plotting characteristics against slip. Agreement is expected at light load because of the prior adjustment to the *B-H* curve but that agreement extends across the range of slip and confirms the basic operation of the simulation. Similarity between grid and inverter supply is expected but small differences will exist because of the additional voltage drop present in the inverter.

Calculating power loss from the subtraction of output power from input power gives a result with quite wide error bounds. The major contribution to the error bounds is the expected error in the torque readings. The experimental results for power loss are shown in figure 3 which also shows the error bounds. Also shown in the figure are the total machine losses found by simulation at four values of slip. In all cases, the simulation results lie within error bounds of the experimental results. At full load the results are at the limit of the range of experimental error. Importantly from the point of view of the objectives of this study, the same trend of power loss against slip is observed for inverter operation over grid operation.

There are several factors for which there is uncertainty and this makes achieving closer agreement difficult. The absence of an accurate rotor temperature estimate and uncertainty over the materials properties such as the conductivity and manufacturing variation of the dimensions of the aluminium rotor bars are the primary concerns. Although the *B-H* curve of the steel was scaled to give agreement of the no-load line current, there is remaining uncertainty over the exact shape of the curve and there was no account taken of degradation of material properties in regions of the laminations that have been work hardened during manufacture.

Figure 4 confirms that the simulation model of the inverter accurately represents the power loss observed in the experiment. The error bars on the simulation results indicate the range of minimum to maximum parameter values quoted by the semiconductor manufacturers.

6 Analysis of Losses

The experimental method presented in section 4 is not able to separately identify machine losses as hysteresis, eddy-current or ohmic, nor separately identify switching and conduction losses in the inverter. But the results of section 5 have verified that the total losses predicted by the

simulation are in agreement with the total losses found by experiment. It is now reasonable to separate out the different terms in the simulation data.

6.1 Relative Importance of Loss Categories

A series of simulations were conducted at slip frequencies between 0.5 and 2.5 Hz for both grid and inverter supply. The losses were categorised as inverter loss and iron or ohmic loss for stator and rotor. The results are plotted in figure 5. As expected, the iron losses and inverter losses are reasonably independent of load (slip) whereas the ohmic losses are approximately quadratically dependent on slip (for these small values of slip).

Ohmic losses for grid and inverter supply are very similar as is expect from the fact that the line currents under these two forms of supply differ by only low magnitude component at high-frequency. This is discussed further in section 6.2.1.

The iron loss, and in particular the rotor iron losses, increases for inverter supply over grid supply. This is true even at light load where stator current is composed mainly of magnetising current. For this relatively small machine, the copper losses are larger than the iron losses. As a consequence, the increase in iron loss for inverter supply does not give a large increase in total losses.

Further evidence that the increase in iron loss caused by inverter supply is much more significant than the increase in ohmic loss is presented in figure 6. The figure shows that the increase in total machine loss found from the experimental data is almost entirely account for by the increase in iron loss determined from the simulation data.

Under grid supply the total loss is 430 W when supplying 2.1 kW giving a full load efficiency of 83.0%. Inverter supply creates around 30 W (1.2% of full load output power) of additional iron loss and 70 W (2.8%) of additional loss in the inverter itself. The efficiency under inverter supply is, therefore, 82.8% for the machine alone, 96.2% for the inverter and 79.8% for the drive as a whole. The somewhat poor efficiency of the inverter is attributed to using IGBTs with a rather low DC-link voltage. The IGBT on-state voltage was in the region of 3.5 V and the DC-link voltage was 400 V.

Within the iron loss category there are sub-categories that are revealed in figure 7. Generally the iron loss is independent of slip but the rotor hysteresis loss does increase with slip frequency. Inverter supply causes an increase in all forms of iron loss but the largest increase is in rotor eddy-current loss. This term accounts for 14 W of the additional 30 W. Stator eddy-current loss accounts for a further 6W.

6.2 Space and Frequency Distribution of Losses

The iron losses in an induction machine are not evenly distributed throughout the lamination cross-section. Iron losses concentrate in the regions of highest flux density, such as the tooth tips. The various second-order contributions to the complete magnetic field, such as leakage flux and space harmonics, concentrate in different physical locations to the main magnetising flux. The time-step data generated by the simulation includes the time record of flux density for every element. This allows iron losses to be plotted as functions of position and frequency. Some locations show high sensitivity to certain frequency components. For this reason, space and frequency distribution of losses are discussed together.

Ohmic losses, on the other hand, have been treated in a straight forward manner. Skin effect has not been accounted for in the stator because of the small wire diameter and skin effect in the rotor used a simple correction factor. Inter-bar currents were not modelled. Thus, only outline comments on ohmic losses are possible.

There are two reasons that spectrum of a machine current (or flux) is other than single frequency: non-ideal machine properties and distortion of the supply itself. Non-linear machine effects include saturation (which causes low-order harmonic distortion) and slotting (which causes modulation products). The PWM waveforms contain carrier and sideband voltage components in addition to the fundamental but negligible low-order harmonic distortion. Figure 8 shows an example frequency spectrum of line current that demonstrates these features for the case of inverter supply.

As noted in section 3, it is important that there are there are no significant amplitude spurious components introduced into the current or flux waveforms by the variable time-step or the reluctivity update process. All of the components in figure 8 that lie above -57dB have been identified as being explained by a feature if the machine, such as a particular slotting component

and no significant spurious components are observed. Below this level, there are many small components that are believed to arise from various features of the numerical solution. Similar patterns emerge in the flux data for individual elements.

In the simulation study, the grid supply was assumed to be perfectly sinusoidal whereas the laboratory supply is known to contain low-order harmonic distortion.

For the purpose of assessing the contribution of the PWM components to the losses, the spectrum was divided into four bands defined as:

- band A [0 - 2.5 kHz) contains the fundamental frequency, low-order harmonic distortion and the most significant slotting components;
- band B (2.5 - 7.5 kHz), the sidebands components of the switching frequency;
- band C (7.5 - 12.5 kHz), the sideband components of the second multiple of the switching frequency;
- band D (12.5 - 17.5 kHz), the sideband components of the third multiple of the switching frequency.

6.2.1 Ohmic Loss

Table 1 shows the stator and rotor ohmic losses (rounded to the nearest integer) for grid- and inverter-based supply across a range of values of slip. The difference between the two types of supply is marginal as expected. Figure 8 showed that the largest additional current component introduced by the PWM was 30dB below the fundamental component.

Figure 9 shows the relative contribution of bands A to D to ohmic losses in the stator and rotor (expressed as a percentage of total ohmic loss in either the stator or rotor. Band A contribution is by far the dominant contribution even for inverter supply (99.88% of stator ohmic loss and 92.5% of rotor ohmic loss for inverter supply) and is off the scale of figure 9. For grid supply the contributions of bands B and C are negligible but not quite zero because of high-order slotting components. Expressed in percentage terms, the rotor ohmic loss in bands B to D are higher under light load than full load. This is largely because the fundamental component of rotor current has reduced rather than because the high frequency content has increased.

For the stator, which has a simple stator resistance without skin effect, the spectrum of the ohmic loss should follow the spectrum of the current. Indeed, figure 9 shows band B contributes 0.1% which matches the -30 dB amplitude of the first order PWM sidebands in figure 8. It is clear that currents in bands B and C make an identifiable but small contribution to ohmic loss.

The rotor current is subject to deep-bar effects that concentrate high frequency currents in the parts of the bar closest to the surface and thus increase the effective resistance of the bar at these frequencies. Thus the rotor power losses shown in figure 9 record a greater contribution in bands B to D than is suggested by the current spectrum.

Notwithstanding the increase in ohmic loss due to inverter supply identified in figure 9, these results, and those of figure 6, show that the extra ohmic loss is small even to the point of being negligible. This is in contrast to the findings in [16, 17]. It is believed that the switching frequency used is the significant difference. In [16], the rotor loss in a 15 kW machine increased by around 300 W for six-step inverter operation over sinusoidal supply and by 400 W for PWM inverter operation. This occurred for all slips up to 0.03. The six-step inverter is expected to produce large amplitude, low-order harmonic distortion in the line current so increased ohmic loss is also expected. The PWM inverter is expected to be free of low-order harmonic distortion but the inverter switching waveforms shown indicate a switching frequency of approximately 1 kHz. Significant current flow will result from PWM sideband components close to 1 kHz.

The simulation and experimental results presented in this paper used 5 kHz PWM. The fivefold increase in frequency is expected to give approximately five times less current distortion due to the low-pass filter characteristic of the machine and, consequently, 25 times less ohmic loss due to that distortion. Taking the 400 W increase in [16] and scaling to account for the frequency difference and difference in machine rating would suggest an increase in rotor loss of approximately 2.2 W in our 2.1 kW machine. The increase found here was smaller still but the remaining difference could be contributed to by detailed differences between the two machines and simulation approaches used. This simple calculation reinforces the point that the difference in switching frequency accounts for most of the difference between the result found here and those in [16].

A large increase in rotor ohmic loss resulting from inverter supply was also reported in [17]. No information is given on the form of inverter switching employed but the current waveforms

indicate that this was probably a six-step inverter and comments in [18] support this assumption. In [18] results are also presented for a PWM inverter. These show a doubling of no-load ohmic loss and a negligible increase in full-load ohmic loss. The current waveforms indicate a PWM frequency in the region of 1 kHz.

6.2.2 Hysteresis Loss

All three sub-categories within iron losses have a dependence on the frequency spectrum of the flux density. For the hysteresis loss, the frequency dependency results from both the linear term in f and Laver's Correction Factor (k_{Laver} in equation 2). Laver's Correction Factor is a multiplier that increases the hysteresis loss to account for the presence of minor loops of the B-H curve. Although this correction is dependent on the frequency content of the flux, it is the shape of the curve that counts. The various frequency terms contribute to k_{Laver} in a non-linear fashion and it is not possible to decompose the loss using Fourier analysis.

Figure 10 separately shows the hysteresis loss in uncorrected form and the k_{Laver} multiplier, both as a function of slip. There is little difference in uncorrected hysteresis loss between grid and inverter supply. This is expected since the peak flux density should be unaltered.

The rotor exhibits the expected dependence of hysteresis loss on slip whereas the stator hysteresis loss is approximately constant. The difference between grid and inverter supply is revealed in the correction factor since the high frequency switching of the inverter is expected to create additional minor loops. In the stator, k_{Laver} is approximately 1.2 for grid supply because of the minor loops caused by slotting. The additional minor loops arising from inverter switching increase this to between 1.3 and 1.4. For the rotor, k_{Laver} is much larger and shows much larger variation with slip. For grid supply it ranges from 13 to 30. For inverter supply this increases to a range of 20 to 45. These very large correction factors indicate a large number of minor loops of significant amplitude.

The values of k_{Laver} found in the rotor (for both grid and inverter supply) need to be treated with caution since they lie outside the range for which Laver provided verification of the correction factor against experimental data. Lavers' work [19] was based experimentally on a 60 Hz sinusoidal waveform distorted by a 20% harmonic component. The harmonic order applied in each experiment was between 3 and 11. With this level of distortion, correction factors between 1.0 and 1.7 were obtained and verified. The correction factor depended on the order of the

harmonic and its phase-shift with respect to the fundamental because both of these aspects affect the shape of the minor loops.

6.2.3 Eddy-Current Loss

For eddy-current loss, the dependence on frequency comes from the rate-of-change of flux density term. In the equation for loss adopted here, equation 3, the term appears squared and so the function is similar to other square law power dissipation functions. Thus, it is possible to decompose the loss into independent frequency terms because they are orthogonal, *i.e.*, products of dissimilar frequencies integrate to zero. Strictly this integral is only zero for rationally related frequencies over a period T which is a common multiple of the periods of each frequency term. Slotting components will not be rational multiples of the supply frequency and the switching frequency might not be either but the error involved is small if the period is large. Conversion to the frequency domain was accomplished with a discrete Fourier transform (DFT) as befits a non-uniformly sampled discrete time system.

It was found that there was a noise floor in the flux density spectrum at around -60dB similar to the noise floor shown in the current spectrum of figure 8. The noise is attributed to small numerical errors in the FEA and time-step processes. Although individually small, the large number of frequencies bins containing noise made a significant, but false, contribution to the calculated loss. It was decided to exclude all components below -57dB so that the effects of switching frequency components were properly revealed. The results were reasonably insensitive to the exact choice of floor applied. Thresholds from -50 to -60dB were tried with no noticeable difference.

Because of the wide variation in the spectrum of the flux density between different elements of the mesh, aggregate figures for the frequency spectrum of the eddy-current loss of the whole machine can hide important detail. Twelve elements representing different regions of the machine were selected as examples. The elements are identified in figure 11.

It is well known that for a typical machine, the flux density in the stator tooth tip is higher than for other regions of the stator and that iron loss will be high in that region because the rate-of-change of flux density (with respect to time) is high in both the tangential and radial directions. Figure 12 shows the loss for the stator elements and it can be seen that the low frequency (band

A) loss in the stator tooth (element 1) is much higher than for other elements (and consequently plotted to a different scale to that used for elements 2-5).

Generally, the loss contribution from inverter switching decreases in the direction from air-gap to back-iron. The high-frequency component of loss appearing in the spectrum at multiples of the switching frequency (bands C and D) are significantly smaller than the loss caused at the switching frequency itself (band B). Although eddy-current loss is proportional to frequency squared, it is the decrease in flux amplitude with frequency (because of the voltage excitation of an inductive circuit and lack of penetration deep into the lamination) that is more important. There is no contribution to loss by the inverter below the switching frequency (band A).

There is an interesting difference between elements 4 and 5 which occupy apparently identical positions toward the base of adjacent stator teeth. Element 5 shows a much higher loss at the switching frequency (band B). There is, however, a difference between these two slots. The stator winding is a simple single-layer winding with three slots per phase. Element 4 is in a tooth in the middle of a phase-band whereas element 5 is in a tooth that falls between two phase-bands. Thus element 5 is subject to the extra phase-band leakage flux produced by the switching frequency voltage components whereas element 4 is not. The extra leakage flux makes a noticeable contribution to eddy current loss.

Figure 13 shows the eddy-current power loss for the seven example rotor elements. It is noticeable that there is a loss contribution in band B even for the grid supplied case. This occurs because the slotting components in the rotor had significant amplitude even at these relatively high frequencies. Following a similar pattern to the stator, the rotor exhibits a decrease of loss in the direction from air-gap to shaft and a small contribution from bands C and D.

The interesting feature of these plots is that in the rotor tooth (but not the tooth tip), elements 9 and 10, the switching frequency components make a higher contribution than the low frequency components. It is worth noting that high pole-number parasitic fields, such as slotting components, do not penetrate deep into the rotor [20] whereas low-pole number parasitic fields, such as induced by inverter switching, appear to penetrate significantly and cause loss across a wider area of the lamination.

6.2.4 Anomalous Loss

Anomalous loss is dependent on the frequency content of the flux density (equation 4). However, because the flux derivative term is raised to the power 3/2, terms involving the product of two different frequencies arise and these do not all integrate to zero over the common period. Thus, it is not possible to separate out the loss contribution of each component in a frequency spectrum of the flux. General trends in the physical location of loss will be similar to those for eddy-current loss because the two types of loss share the term *dB/dt* raised to a power (3/2 in the case of anomalous loss and 2 in the case of eddy-current loss).

6.2.5 Relative increase in total iron loss

Figure 14 and figure 15 show the relative increase in total iron loss across the stator and rotor laminations (respectively) when the supply is changed from grid to inverter. The change is expressed as a percentage of the loss found under grid excitation on an element-by-element basis. The machine was operated under rated load. The most obvious feature of figure 14 is the increase in loss caused by phase-band leakage flux at the switching-frequency (as described in section 6.2.3). The teeth between phase-bands show an increase in iron loss of around 70% whereas teeth in the middle of phase-bands show a modest increase of around 10-20%. The tooth tip regions, which are already subject to the highest losses, show an increase of 30-40%.

Figure 15 reveals that the highest increase in iron loss in the rotor occurs near the head of the rotor bar. This region is the region of secondary slot leakage discussed by Alger [3]. (Note that the scale for the rotor extends to 150% whereas that for the stator it extended to 100%). Along the tooth sides the increase in loss is 55-65%. Although this is less than found at the head of the bar, it is still a significant increase.

High frequency leakage flux has been found to make an important contribution to the additional loss resulting from inverter supply in both the stator and the rotor. In equivalent circuit terms, the leakage impedances are relatively low impedance paths current driven by switching frequency components of the supply voltage.

The increase in rotor iron loss found here has occurred with only a small increase in rotor ohmic loss. There are several factors that can explain this observation. First, additional high frequency terms contribute to the ohmic loss through the magnitude (of the current term) whereas they contribute to iron loss through the time derivative (of the flux term) raised to some power. Low

amplitude high frequency currents will have a small effect on ohmic loss but can have a significant impact on iron loss. Second, flux crossing the air-gap from the stator can create iron loss in the rotor surface without the presence of rotor current. The extent to which high frequency flux will penetrate into the depths of the rotor depends on the material properties of the rotor and the distribution of any induced rotor current. There are some limitations in the model used here that need to be acknowledged. The assumed uniform distribution of current in the rotor bars will lead to inaccuracy in the modelling of the penetration of high frequency flux into the rotor (although skin effect is accounted for in rotor ohmic loss). Neglecting the space harmonics of the rotor current distribution may have caused some inaccuracy. These factors will also have affected the results shown in figure 13. The figure does show that the PWM related fields are attenuated from rotor surface to rotor core but to some extent the loss in the elements near the surface may still be understated and the loss overstated in those elements alongside the bar. Despite the limitations, it is believed that the results are a reasonable representation of the phenomena in the machine and indicate well the distribution (in terms of category, frequency and location) of additional loss caused by the inverter.

7 Conclusions

The simulation technique employed in this work has two important characteristics: a variable time-step and a strategy to reduce the update rate of the lamination reluctivity. These two actions proved to be successful in providing a computationally efficient simulation process without losing the information contained in the short-duration pulses of the PWM inverter waveforms. The accuracy of the simulation was assessed against experimental data. For both grid and inverter supply there was agreement (to within the accuracy of the instrumentation) between simulation and experiment for line current and power loss. With the accuracy of the simulation scheme established, the simulation data for power loss was examined in detail. The assessment covered the contribution of the switching and conduction losses of the inverter and the ohmic and iron losses in the motor.

For the ohmic losses, the difference between grid and inverter excitation was found to be negligible. The low-pass filter characteristic of the induction machine attenuates significantly the PWM carrier and sidebands of the inverter supply voltage such that the additional current and additional loss are both small.

The analysis of iron losses was the main focus of the study since this aspect has many unresolved issues for inverter-supplied machines. Iron losses were divided according to their nature into hysteresis, classic eddy-current and anomalous losses. There was found to be little difference in hysteresis losses between the two types of supply. The differences that did exist arose in Lavers' correction factor. This correction factor must be treated with caution, particularly for the rotor, since the flux density waveforms have a degree of distortion much higher than in Lavers' original study.

The iron losses were found to be about 50% higher for inverter supply rather than grid supply. This increase is mainly due to the eddy current loss. The eddy current loss was partitioned by frequency band for each element of the FEA mesh. In the frequency domain, the most important aspect is the impact of the sidebands around the switching frequency. Some contribution from the sidebands of the second multiple of the switching frequency is also observed. The extra loss produced by inverter supply varies by location and saturation level. The highest increase in loss is found near the head of the bars in the rotor and in the tooth forming the phase-band boundary in the stator. In both locations, additional leakage flux created by the sidebands in PWM voltage waveform is an important contribution.

A further aspect of the study that needs to be treated with caution is the iron loss modelling in the presence of high frequency fields. In this study the flux density is assumed to be uniform through the thickness of the lamination. This may not be accurate for fields created by high frequency switching (or the high switching frequency multiplies of low frequency switching). This aspect of iron loss has received very little attention to date.

8 Acknowledgements

The authors are indebted to Dr C.I. McClay (of Edison Mission Energy, Chester, UK) for the wealth of experience on time-step FEA simulation and induction machine design that she shared during the course of this work. Mr. Hernández-Arámburo wishes to thank *Consejo Nacional de Ciencia y Tecnología – México* for funding his Ph.D. programme at Imperial College.

9 References

1 W. Prescott, D. G. Watterson, M. Bradford and M. Lockwood, “Computational methods for the steady-state performance prediction of cage induction motors fed from non-sinusoidal supplies”, IEE Conf. on Electrical Machines and Drives, pp 271-274, 1989

2 B. A. Behrend, *The Induction Motor*. McGraw Hill, 2nd Ed., 1921.

3 P. L. Alger, *Induction Machines: Their Behaviour and Uses, Gordon and Breach Publishers*, 2nd Ed., 1995.

4 R. C. Healey, S. Williamson, and A. Smith, “Improved cage rotor models for vector controlled induction motors", IEEE Trans. on Industry Applications, Vol. 31, pp. 812-822, July/August 1995.

5 E. Levi, “Impact of iron loss on behavior of vector controlled induction machines", IEEE Trans. on Industry Applications, Vol. 31, pp. 1287-1296, November/December 1995.

6 N. E. Hildebrand and H. Roehrdanz, “Losses in three-phase induction machines fed by PWM converter", IEEE Trans. on Energy Conversion, Vol. 16, pp. 228-233, September 2001.

7 H. Rapp, “Examination of additional rotor-losses in inverter-fed induction machines", International Conference on Industrial Electronics, Control and Instrumentation, Vol. 2, pp. 881-886, 1993.

8 K. Atallah, Z.Q. Zhu and D. Howe, “An improved method for predicting iron losses in brushless permanent magnet DC drives”, IEEE Trans. on Magnetics, Vol. 28, No. 5, pp. 2997-2999, 1992

9 M. A. Mueller, S. Williamson, T. J. Flack, K. Atallah, B. Baholo, D. Howe, and P. H. Mellor, “Calculation of iron losses from time-stepped finite-element models of cage induction machines", IEE Conf. on Electrical Machines and Drives, Vol. 1, pp. 88-92, IEE, September 1995.

10 R. Findlay, N. Stranges, and D. MacKay, “Losses due to rotational flux in three phase induction motors”, IEEE Transactions on Energy Conversion, Vol. 9, No. 3, pp. 543-549, 1994.

.

11 C.A. Hernandez-Aramburo, T.C. Green and A.C. Smith, “An estimation of rotational iron losses in an induction machine”, Submitted to IEEE Transactions on Magnetics.

12 N. Allen, H.C. Lai, P.J. Leonard and D. Roger, “External circuit movement and periodicity considerations in the design of electrical machines using finite elements”, IEE Conf. on Electrical Machines and Drives, pp. 126-130, 1995.

13 C. I. McClay and G. T. Van der Thorn, “A comparison of time-stepped finite element techniques for the calculation of losses in cage induction motors", IEE Conf. on Electrical Machines and Drives, Vol. 1, pp. 35-39, September 1999.

14 S. Williamson, L. H. Lim, and M. J. Robinson, “Finite element models for cage induction motor analysis", IEEE Trans. on Industry Applications, Vol. 26, pp. 1007-1017, 1990.

15 S. Mukherjee, G. E. Adams, and R. Hoft, “FEM analysis of inverter-induction motor rotor conduction losses", IEEE Trans. on Energy Conversion, vol. 4, pp. 671-677, 1989.

16 A. Arkkio, “Finite element analysis of cage induction motors fed by static frequency converters", IEEE Trans. on Magnetics, vol. 26, pp. 551-554, 1990.

17 J. F. Bangura, F. N. Isaac, N. A. Demerdash, and A. A. Arkadan, “A time-stepping coupled finite element-state space model for induction motor drives. Part 2: machine performance computation and verification," IEEE Electric Machines and Drives Conf., pp. WB3/4.1-WB3/4.3, 1997.

18 N.A.O. Demerdash and J.F. Bangura, “Characterisation of Induction Motors in adjustable-speed drives using finite-element state-space method including experimental validation”, IEEE Trans. on Industry Applications, Vol. 35, No. 4, pp 790-802, 1999.

19 J. D. Lavers, P. P. Biringer, and H. Hollitscher, “A simple method of estimating the minor loop hysteresis loss in thin laminations", IEEE Trans. on Magnetics, Vol. MAG-14, pp. 386-388, September 1978.

20 C. I. McClay, *Efficiency improvement of cage induction motors*, PhD thesis, St John's College, The University of Cambridge, February 1996.

10 Tables

		Slip [Hz]			
		2.5	2.0	1.25	0.50
Stator	Grid	241	191	129	99
	PWM	242	192	131	99
Rotor	Grid	137	95	46	13
	PWM	139	96	46	13

Table 1 Ohmic power losses [W]

11 Figures

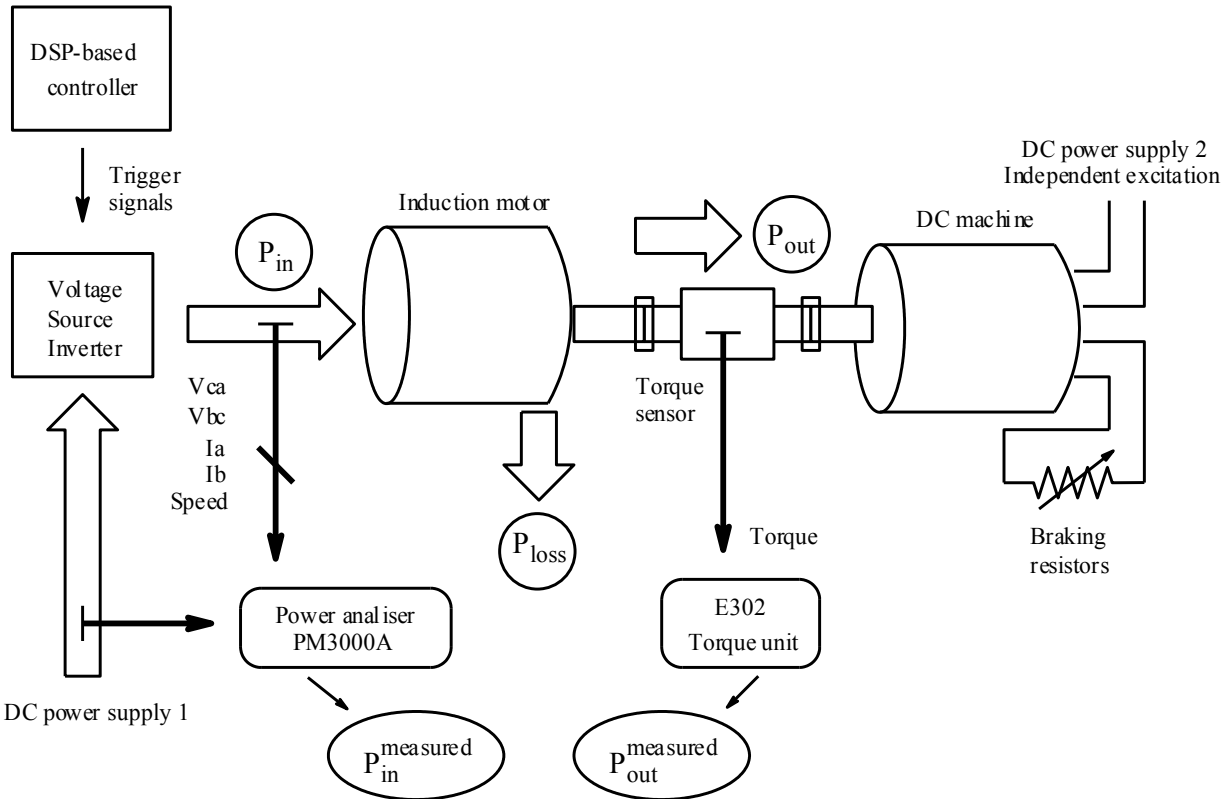

Figure 1 Block diagram of the experimental test system.

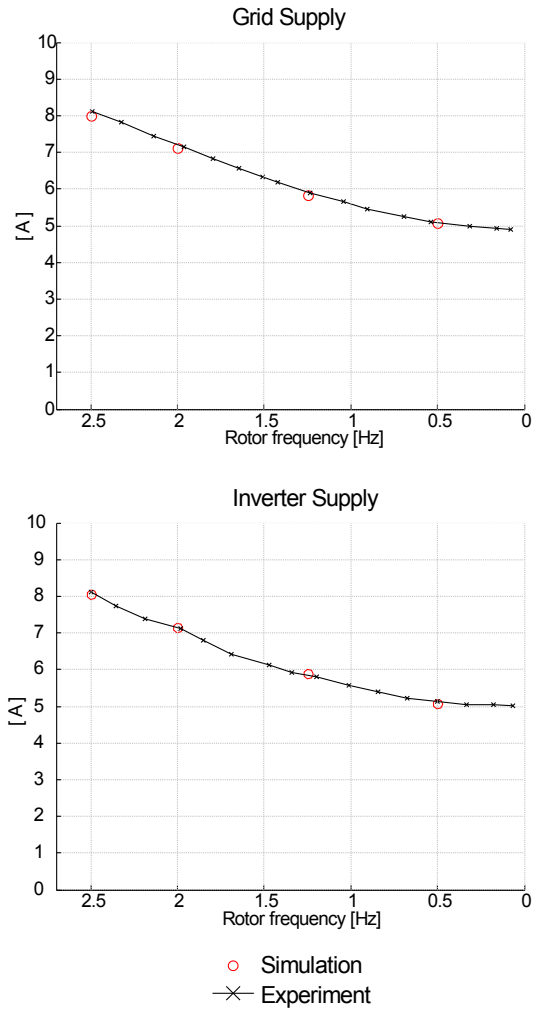

Figure 2 Experimental and simulation results for stator current for both grid and inverter supply.

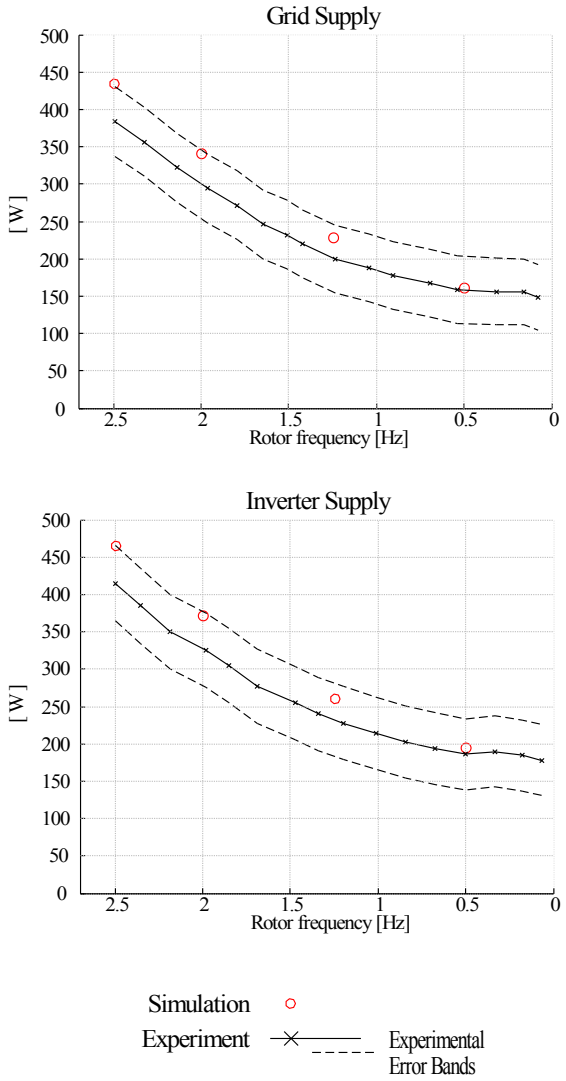

Figure 3 Power loss in the induction machine

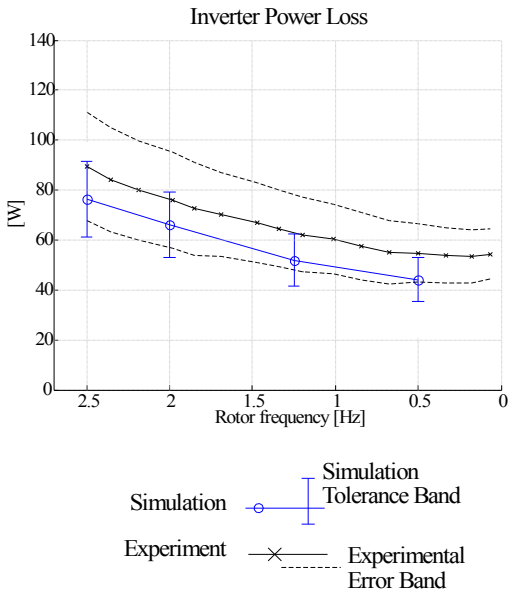

Figure 4 Power loss in the inverter

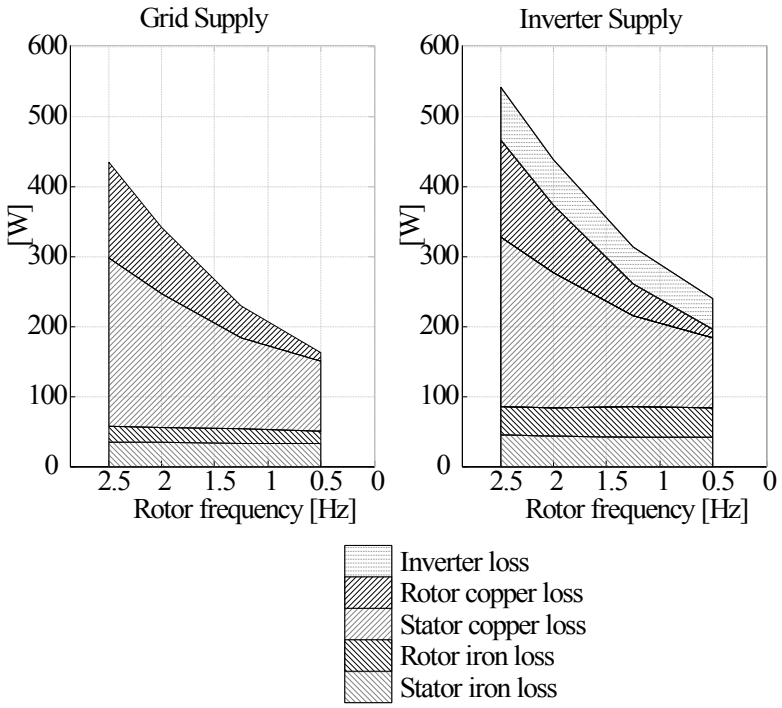

Figure 5 Iron, ohmic and inverter losses for grid and inverter supply as a function of slip frequency.

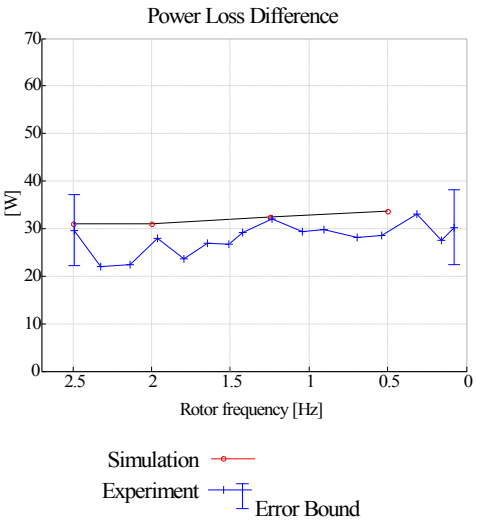

Figure 6 Additional loss of inverter supply over grid supply: measured increase in total machine loss and simulated increase in iron loss.

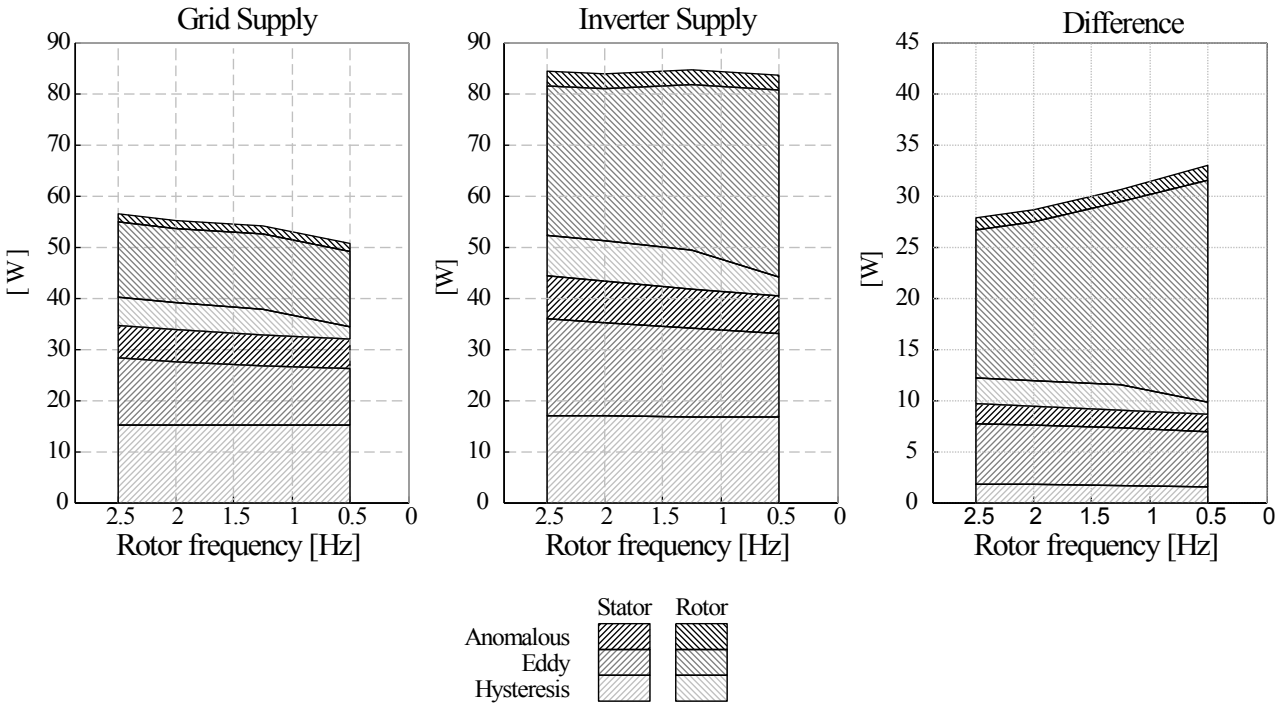

Figure 7 Iron losses under grid and inverter supply as a function of slip.

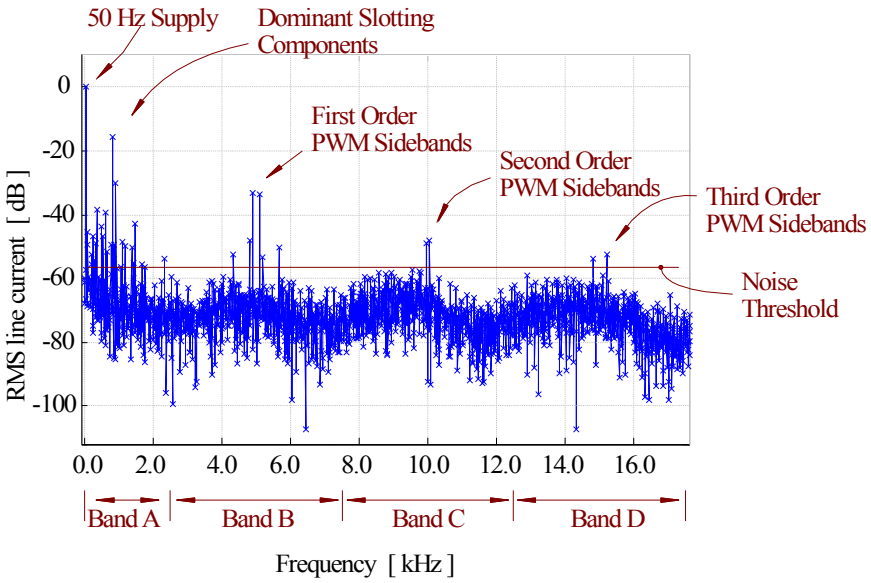

Figure 8 Example spectrum of the line current of the induction machine.

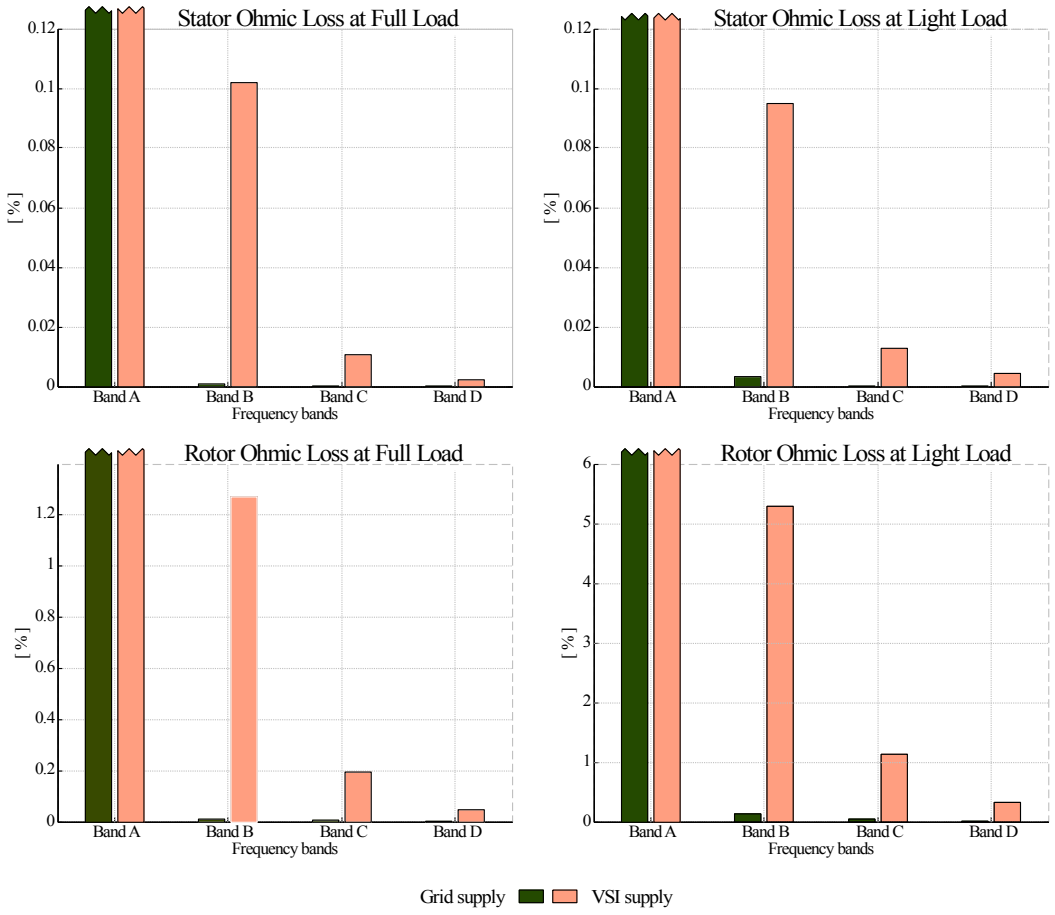

Figure 9 Stator and rotor ohmic losses at light and full load by frequency band. Band A power loss is dominant and exceeds these axes. Band A accounts for 99.88% of stator ohmic loss and 92.5% of rotor ohmic loss.

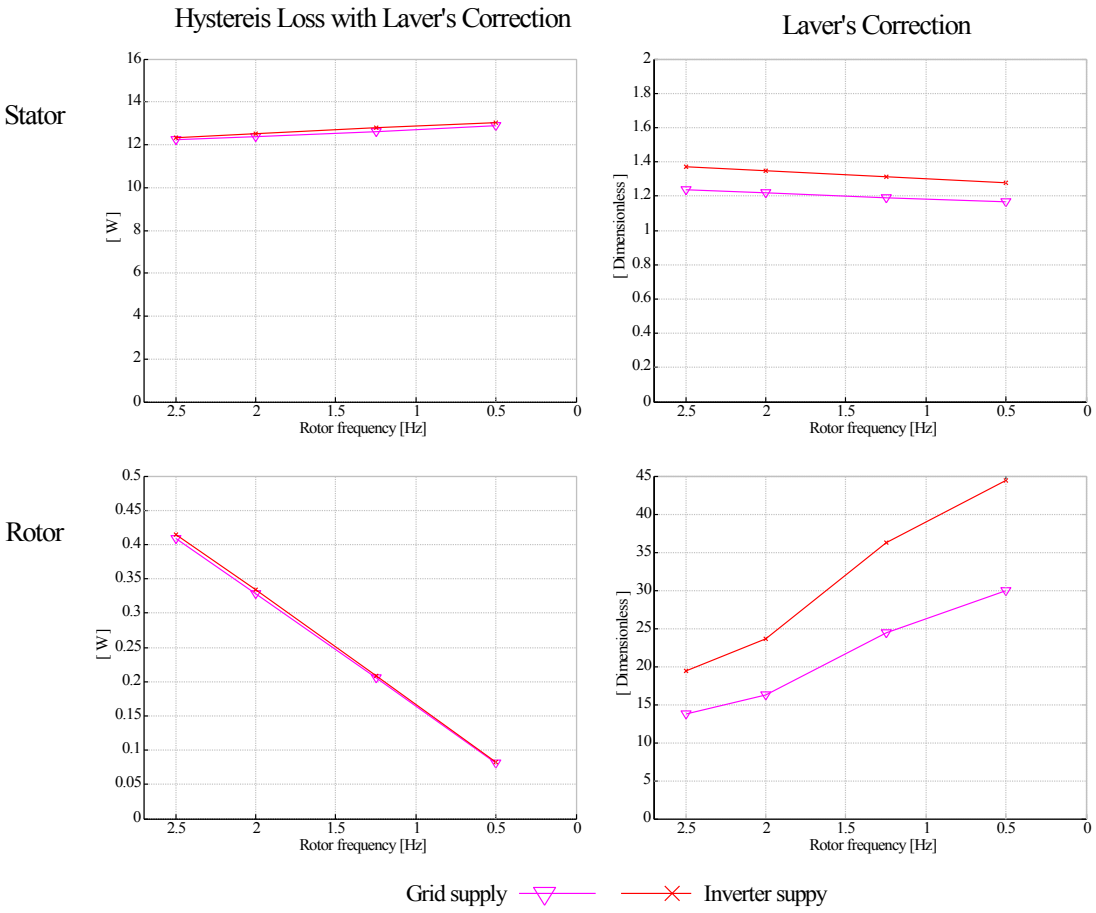

Figure 10 Hysteresis loss calculated without a correction for minor loops and, separately, Laver's Correction Factor.

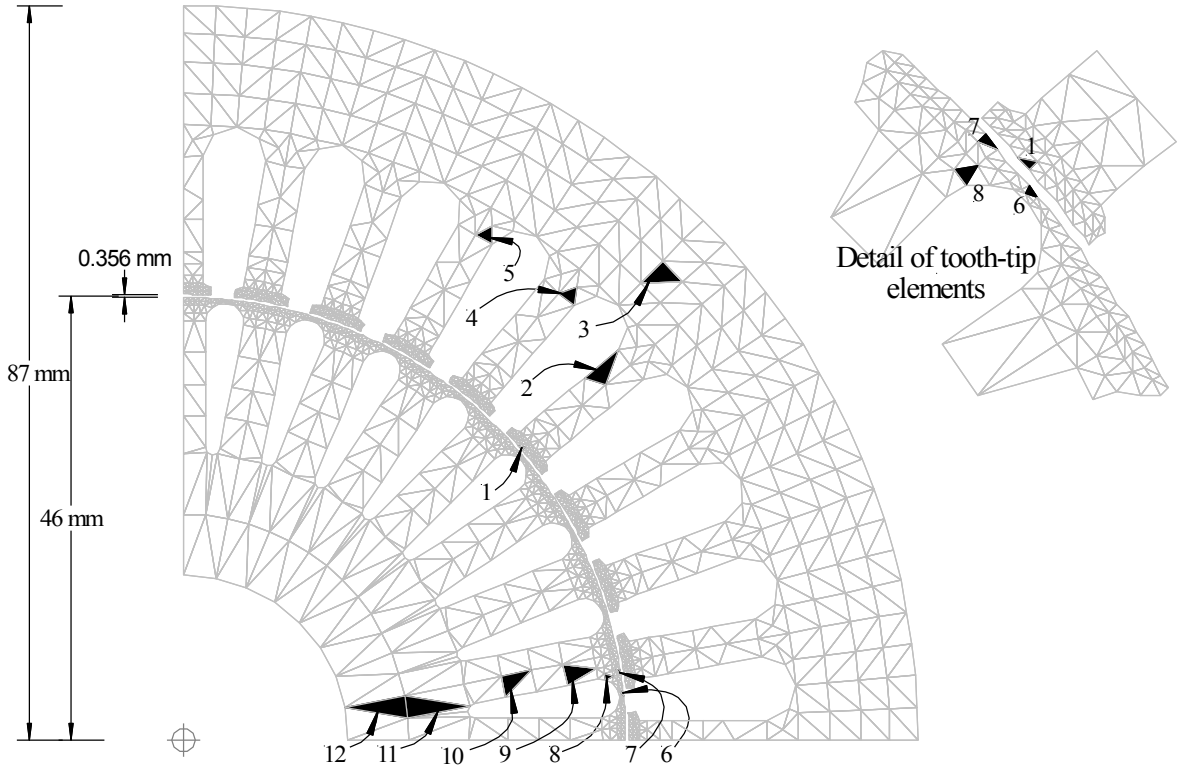

Figure 11 The mesh for stator and rotor (but not air-gap) laminations showing the location of the 12 example elements: 5 in the stator and 7 in the rotor.

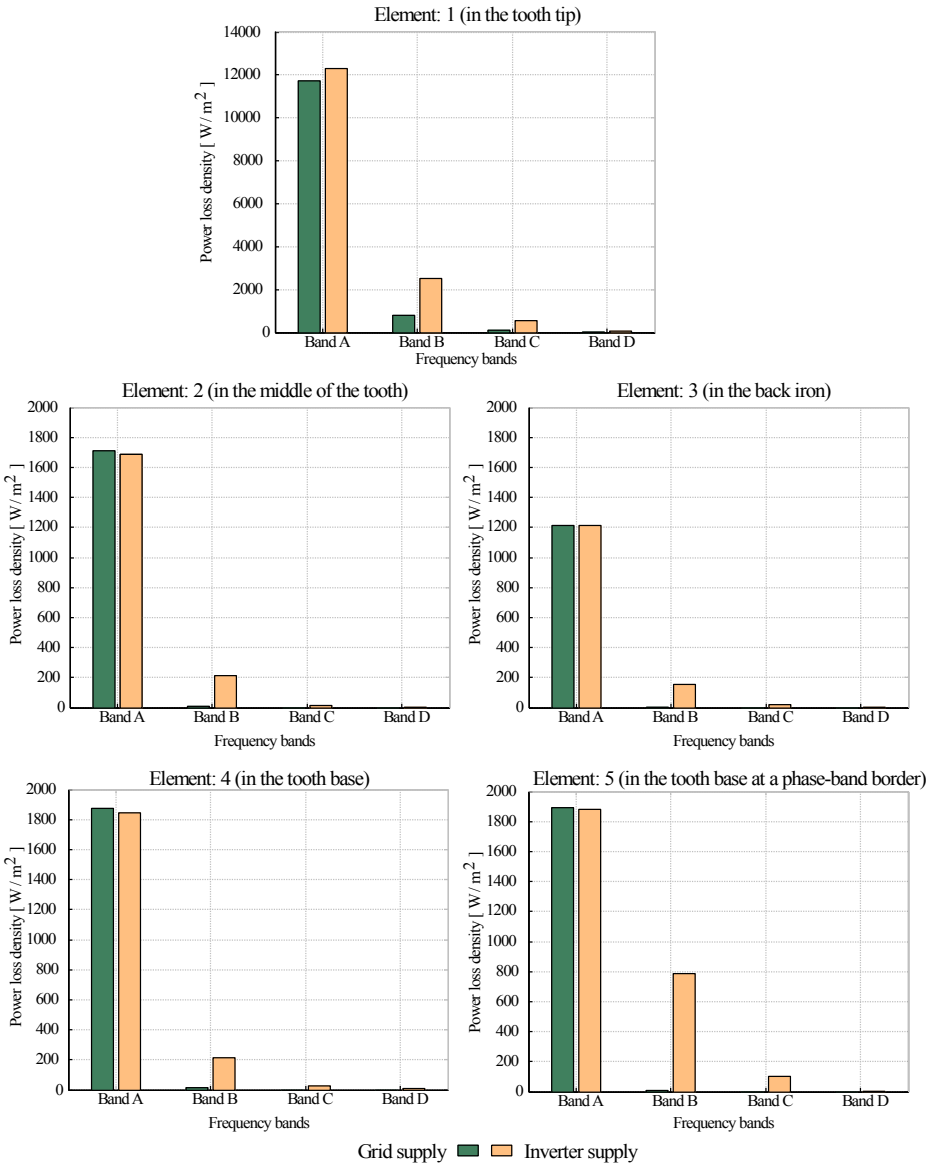

Figure 12 Eddy-current power loss by frequency band for the five example elements in the stator. (Note that the loss for element 1 is plotted to a different scale to that for elements 2-5.)

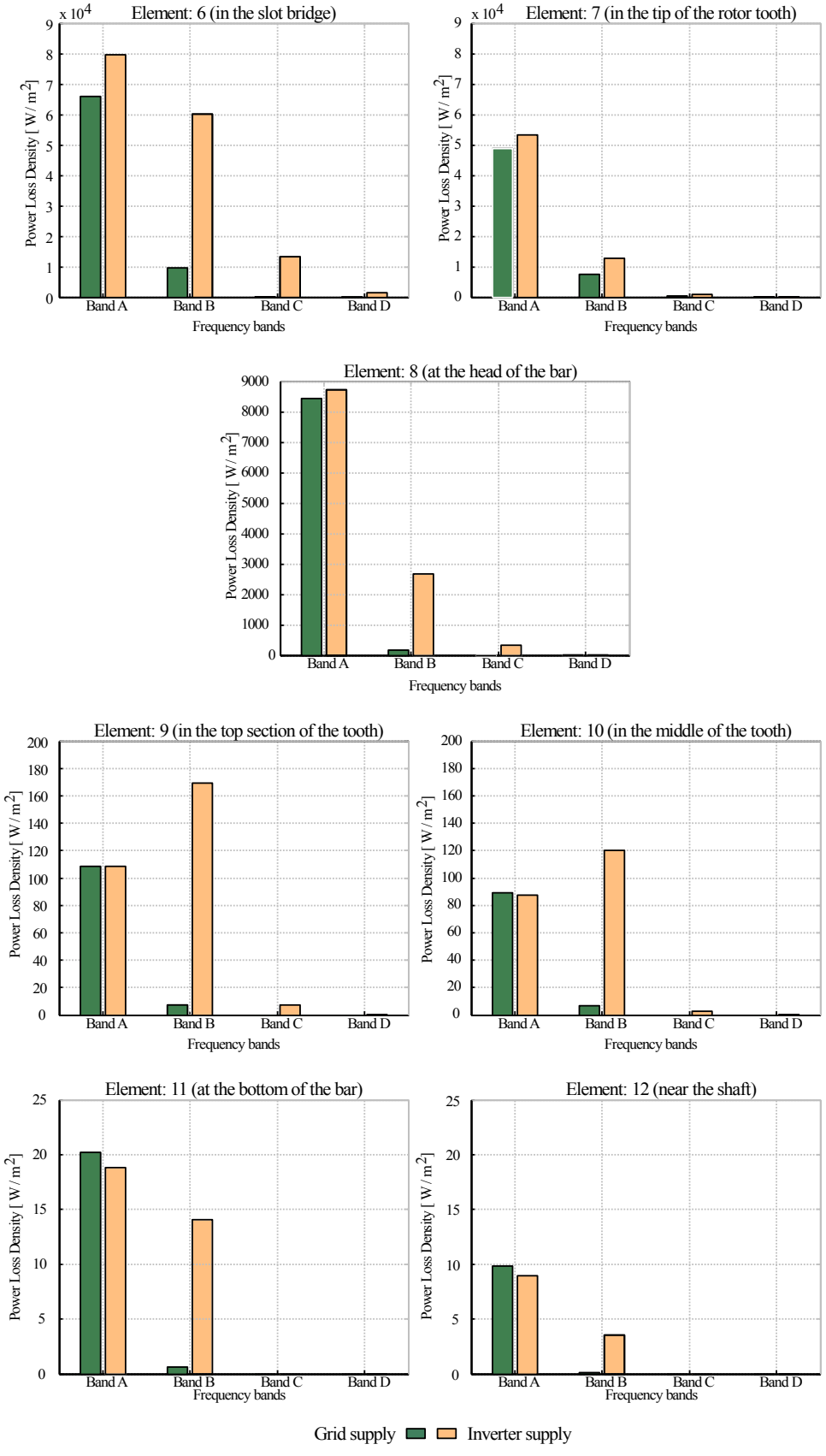

Figure 13 Eddy-current power loss by frequency band for the seven example elements in the rotor.

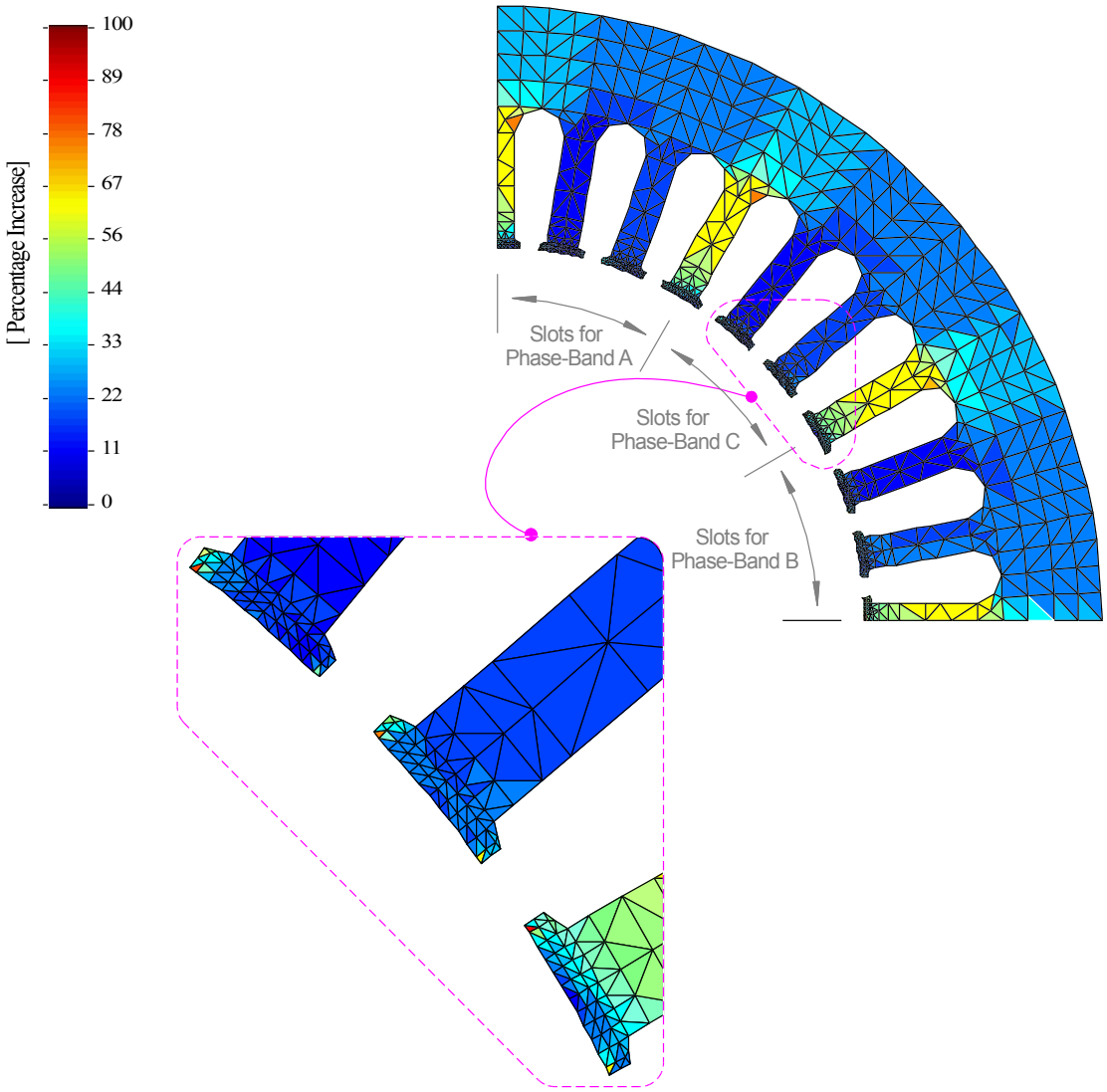

Figure 14 Relative (percentage) increase in iron loss in the stator due to inverter supply.

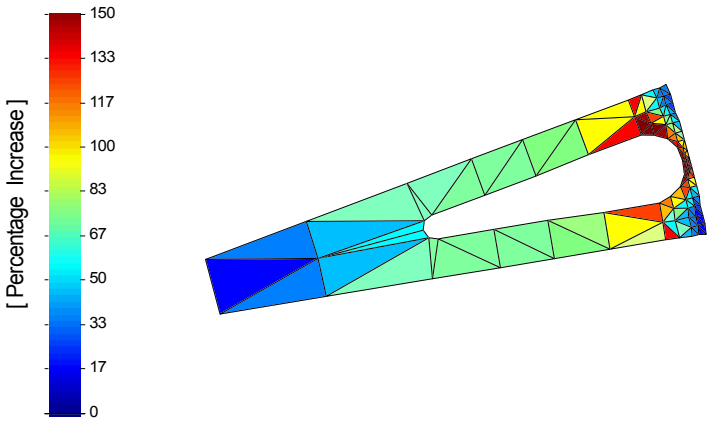

Figure 15 Relative (percentage) increase in iron loss in the rotor due to inverter supply